

Silician magnetite from the Dales Gorge Member of the Brockman Iron Formation, Hamersley Group, Western Australia

JASON M. HUBERTY,* HIROMI KONISHI, PHILIPP R. HECK,† JOHN H. FOURNELLE, JOHN W. VALLEY, AND HUIFANG XU

NASA Astrobiology Institute, Department of Geoscience, University of Wisconsin-Madison, 1215 West Dayton Street, Madison, Wisconsin 53706, U.S.A.

ABSTRACT

We report silician magnetite from banded iron formation (BIF) in the Dales Gorge Member of the Brockman Iron Formation, Hamersley Group, Western Australia. Magnetite mesobands typically consisting of individual ~100 μm microlaminae are revealed to be composed of silician magnetite overgrowths on magnetite. Silician magnetite overgrowths contain from 1 to 3 wt% SiO_2 , whereas (low-Si) magnetite domains contain less than 1 wt% SiO_2 . Silicon solid solution is present in the magnetite crystal lattice as determined by in situ micro-X-ray diffraction and high-resolution transmission electron microscopy. Three textures are distinguished in magnetite mesobands: (1) magnetite sub-microlaminae with silician magnetite overgrowths, (2) recrystallized magnetite fragments with silician magnetite overgrowths, and (3) a complex intergrowth of magnetite and silician magnetite. All three textures are found in magnetite mesobands from the BIF4-5 and BIF12-16 macrobands of the Dales Gorge type-section drill core DDH-47A from Wittenoom, Western Australia. Magnetite domains contain numerous submicrometer-to-micrometer inclusions of quartz, carbonate, stilpnomelane, and apatite, whereas silician magnetite overgrowths are devoid of mineral inclusions. The presence of mineral inclusions in magnetite indicates the BIF oxide precipitate was not chemically pure iron oxyhydroxide/oxide. Magnetite domains display textures formed during soft sediment deformation that are the earliest and best preserved relict sedimentary structures in this BIF. Silician magnetite is the dominant iron oxide in the Dales Gorge BIF and is present in many other sub-greenschist facies BIFs worldwide. We suggest the former presence of organic matter creates reducing conditions necessary to stabilize silician magnetite. Thus, silician magnetite is a potential biosignature in BIFs.

Keywords: Magnetite, silician magnetite, banded iron formation, Dales Gorge, Hamersley, biosignature

INTRODUCTION

Magnetite (Fe_3O_4) is a common mineral in many rock types and, with hematite (Fe_2O_3), comprises the major economic source of iron derived largely from banded iron formations (BIFs). BIFs are chemical marine sedimentary rocks with distinctive alternating iron-rich (oxides, carbonates, and sulfides) and silica-rich (chert and jasper) layers. BIFs are defined as having a minimum 15% Fe and have been classified into depositional facies based on the dominant mineralogy (James 1954). Oxide facies BIFs are largely composed of iron oxides and chert (usually in sub-equal amounts) but can also contain numerous other minerals depending on metamorphic grade. Oxide-facies BIFs that have experienced low degrees of metamorphism (sub-greenschist facies conditions) typically contain iron oxides, chert, iron-rich carbonates, stilpnomelane (and other silicates), apatite, rare pyrite, and trace amounts of organic matter (Klein 2005). Magnetite and hematite are not generally considered as direct

BIF precipitates but may form by transformation of precursor amorphous ferric oxides/hydroxides [$\text{Fe}(\text{OH})_3$] by microbial iron reduction in the buried sediment (Konhauser et al. 2005; Johnson et al. 2008; Koehler et al. 2010).

BIFs are enigmatic, highly aesthetic, and an oft-cited example of non-uniformitarianism in the geologic record. For these reasons, and as the dominant economic source of iron, BIFs have been the subject of extensive study. Recent reviews provide an important summary of the current understanding of the formation of BIFs (Trendall 2002; Klein 2005; Ohmoto et al. 2006; Bekker et al. 2010), and advanced analytical techniques are bringing new insight (Johnson et al. 2008; Pecoits et al. 2009; Steinhofel et al. 2009, 2010; Czaja et al. 2010; Heimann et al. 2010; Craddock and Dauphas 2011; Heck et al. 2011), yet much remains unknown since no modern analog exists and most BIFs have undergone at least some degree of metamorphism.

BIFs also provide a unique record of iron and silicon cycling in the Precambrian. The hydrous surfaces of iron hydroxides are known to have a strong affinity for dissolved constituents in seawater including silicic acid (H_4SiO_4) (Harder 1965; Harder and Flehmig 1970; Yokoyama et al. 1980, 1984). Recent experiments have shown that microbial reduction of ferrihydroxide in the presence of silica produces magnetite (Kukkapudu et al.

* E-mail: jason@geology.wisc.edu

† Present address: Robert A. Pritzker Center for Meteoritics and Polar Studies, Department of Geology, The Field Museum, 1400 South Lake Shore Drive, Chicago, Illinois 60605, U.S.A.

2004), and the fractionation of iron isotopes is affected by the interaction of silica with ferrihydrite (Wu et al. 2009). Fischer and Knoll (2009) proposed an “iron shuttle model” where the adsorption of silica to ferrihydrite is a major pathway for the removal of Si from the ocean and deposition thereof in BIFs.

SILICIAN MAGNETITE

At least 32 prior studies (Supplemental Table A1¹) have reported the presence of silician magnetite from a wide range of rock types formed at low to high temperatures: banded iron formation, mid-ocean ridge serpentinite, volcanogenic massive sulfide (VMS) deposits, skarns, and porphyries, felsic to gabbroic igneous rocks, pegmatites, and carbonatites. Those studies report a range in SiO₂ up to 8 wt% for silician magnetite. Shimazaki (1998) distinguished between high-temperature igneous occurrences where silician magnetite also contains several weight percent of other elements (e.g., Ca, Mg, Mn, Al, and Ti) and lower temperature skarn, porphyry, VMS, and serpentinite occurrences where silician magnetite contains more than 1 wt% SiO₂ but is otherwise low in chemical impurities.

The goals of this study are to document magnetite microstructures in detail and characterize the crystal chemistry of silician magnetite in the Dales Gorge BIF. We determine if silicon solid solution is present in the magnetite lattice, evaluate solid-solution models for the formation of silician magnetite, discuss redox conditions during the formation of silician magnetite, and whether silician magnetite is a biosignature.

SAMPLES AND PREPARATION

The petrography of the 2.45–2.50 Ga Dales Gorge Member of the Brockman Iron Formation, Hamersley Group, Mt. Bruce Supergroup (Trendall et al. 2004), is well described in numerous publications (Trendall and Blockley 1968, 1970; Ayres 1972; Morris 1980, 1993; Ewers and Morris 1981; Krapež et al. 2003; Pickard et al. 2004; Pecoits et al. 2009). The different scales of banding in the Dales Gorge Member are described in detail by Trendall and Blockley (1968, 1970) and are briefly summarized here. The Dales Gorge Member is subdivided into 33 macrobands (meter-scale subdivisions) of BIF (BIF0–16) and shale (S1–16) as shown in Figure 1. Macrobands are subdivided into mesobands (alternating centimeter-scale layers). Ayres (1972) described the mineralogy of BIF from the Dales Gorge Member in detail and after Trendall and Blockley (1968), classified six mesoband types based on the dominant mineralogy: iron oxide, chert, quartz-iron oxide, carbonate, stilpnomelane, and riebeckite. Mesobands are subdivided into microbands, sub-millimeter thick layers that are in turn composed of micrometer-scale laminae, or microlaminae. Sub-microlaminae are internal layers contained within single microlaminae (Ewers and Morris 1981).

A microband was originally defined as an iron oxide-quartz couplet and interpreted as an annual layer or varve (Trendall and Blockley 1968; Trendall 1973). These couplets were later renamed afbands since microband has also been used to describe single lamina. Other hypotheses to explain the origin of microbanding in BIFs include density current resedimentation (Krapež et al. 2003), oscillations in hydrothermal activity (Ohmoto et al. 2006), fluctuating temperatures in the ocean photic zone (Posth et al. 2008), and the internal dynamics of coupled Fe and Si cycling linked to

hydrothermal leaching of komatiites (Wang et al. 2009).

The samples in this study are from diamond drill hole (DDH)-47A located ~15 km south of Wittenoom, Western Australia (Zone 50 627013E 7529757N). DDH-47A was used to define the stratigraphic subdivisions of the Brockman Iron Formation, and is the type section core for the Dales Gorge Member (Trendall and Blockley 1968). DDH-47A is currently stored at the Perth Core Library, and polished half-core sections of the complete drill hole are on display as lift panels on the fifth floor of Mineral House in Perth, Western Australia (Blockley et al. 2008).

Our samples are from quarter-core sections of DDH-47A selected by Cornelius Klein in 1978. Klein donated these samples to the Department of Geoscience, UW-Madison, and they are catalogued in the collections of the UW-Madison Geology Museum (UWGM500.xxx). The drill core material was initially thought to be from DDH-44 in Paraburdoo due to a transposition error in the documentation provided with the samples. Johnson et

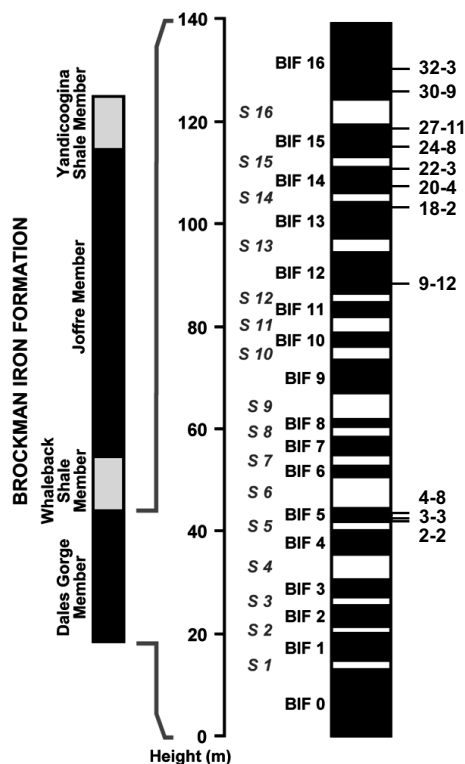


FIGURE 1. Stratigraphic column of the Brockman Iron Formation, Hamersley Group, Mt. Bruce Supergroup, Western Australia. The Dales Gorge Member is subdivided into 33 banded iron formation (BIF) and shale (S) macrobands. Sample numbers (2-2 to 32-3) from drill core DDH47-A (Supplemental Figures A1–A8¹) are shown with respect to stratigraphic placement in the BIF5 and BIF12–16 macrobands.

¹ Deposit item AM-12-004, Supplementary figures and tables. Deposit items are available two ways: For a paper copy contact the Business Office of the Mineralogical Society of America (see inside front cover of recent issue) for price information. For an electronic copy visit the MSA web site at <http://www.minsocam.org>, go to the *American Mineralogist* Contents, find the table of contents for the specific volume/issue wanted, and then click on the deposit link there.

al. (2008) reported Fe isotope data from these samples but were unaware of the misidentification. Subsequently, and thanks to the assistance of Richard Morris, we were able to authenticate our samples as DDH-47A from Wittenoom. Our samples and the associated worksheet photos (Supplemental Figures A1–A8¹) match the photographic plates in Trendall and Blockley (1968, 1970), Morris (1973), and Blockley et al. (2008).

EXPERIMENTAL METHODS

Eleven samples were chosen from 7 BIF macrobands in DDH-47A (BIF4, 5, 12–16), and the sample numbers (2-2 to 32-3) are shown with reference to the stratigraphic subdivisions of the Dales Gorge Member (Fig. 1). Rock chips (millimeter to centimeter in size) were sawed from quarter-core material. Samples were cast in 1 in. epoxy rounds and subsequently ground, lapped, cleaned, and coated with ~20 nm of carbon for scanning electron microscopy. For electron backscatter diffraction analysis, sample mounts were polished for ~1 h with a 0.05 μm colloidal alumina polishing suspension to remove surface damage created by mechanical polishing and then analyzed uncoated by SEM in variable pressure mode.

Scanning electron microscopy

SEM was performed on a Hitachi S-3400N at the UW-Madison under high vacuum (10^{-5} torr) and in variable pressure mode (10^{-1} torr). Energy-dispersive X-ray spectroscopy (EDS) was performed using an accelerating voltage of 15 kV, a working distance of 10 mm, and Thermo Scientific NORAN System SIX software. Backscatter electron (BSE) imaging was performed using a high-sensitivity semiconductor detector located directly above the sample.

Electron backscatter diffraction

EBSD was performed using an Oxford Instruments NordlysS II detector equipped with a phosphor screen. The operating conditions used were an accelerating voltage of 20 keV and high filament saturation with a tight fixed beam. The sample was tilted to 70° from normal to the stage (incident beam 20° from parallel to the sample surface) at a working distance of 23 mm. Electron backscatter patterns (EBSPs) were collected on a phosphor screen using the Oxford Instruments software package CHANNEL5 in point collection and automated mapping modes. Each EBSP has a mean angular deviation (MAD: a measure of the residuals of the simulated EBSP match to the actual EBSP) of less than 1°. Orientation contrast (OC or forescatter) imaging was performed using the Oxford Instruments NordlysS II forescatter detector system. Operating conditions are identical to that used for EBSD. OC images were obtained using two semiconductor detectors located to the side of the sample below the phosphor screen on the EBSD detector. In OC images, contrast is caused by relative differences in crystal orientation, not differences in average atomic number as for BSE.

Electron probe microanalysis

EPMA was performed with a CAMECA SX51 electron microprobe. The operating conditions used were an accelerating voltage of 20 kV, a Faraday cup current of 20 nA, and a tight fixed beam with a diameter of ~1 μm . Natural crystalline standards used were Minas Gerais magnetite USNM 114887 for Fe, Minas Gerais rutile (TiO₂) for Ti, spinel (MgAl₂O₄) for Mg and Al, and gahnite (ZnAl₂O₄) USNM 145883 for Zn. Synthetic standards used were Mn₂SiO₄ for Mn and Si, vanadium metal for V, and Cr₂O₃ for Cr. Data were reduced using the Probe for EPMA software (Donovan et al. 2010), and the matrix correction utilized was the Armstrong-Love/Scott phi-rho-z method (Armstrong 1988) modified from Brown and Bastin with Henke mass absorption coefficients. During the EPMA matrix correction for magnetite, we defined a Fe:O ratio of 3:4. Oxygen was calculated from cation stoichiometry, included in the matrix correction, and the chemical formula was normalized to 4 O atoms. A stoichiometric Fe³⁺:Fe²⁺ ratio of 2:1 was assumed for distributing charge. All reported elements are present above detection limits at 99% confidence levels.

In situ micro-X-ray diffraction

Micro-XRD analyses were carried out using a Rigaku Rapid II X-ray diffraction system with a 2D image plate (MoK α radiation, $\lambda = 0.70928$ Å). Diffraction data were collected on an image-plate detector. The two-dimensional images were integrated to produce conventional 2 θ -intensity patterns using the Rigaku 2DP software. An accelerating voltage of 50 kV was used with a current of 50

mA and a 30 μm diameter collimator. Polished rock chips in 1 in. epoxy mounts were measured in reflection mode.

Transmission electron microscopy

TEM and scanning transmission electron microscopy (STEM) measurements were performed using a FEI Titan 80-200 aberration corrected scanning/transmission electron microscope at 200 kV coupled with an EDAX AMETEK high-resolution EDS detector and Gatan image filtering system. Samples were prepared by crushing magnetite fragments between two glass slides with ethanol. A drop of the suspension was placed on a lacey carbon-coated Cu grid and air dried. TEM samples were lightly coated with ~10 nm of carbon so that magnetite particles were not attracted to the pole piece.

RESULTS

Magnetite and silician magnetite textures

Detailed imaging of magnetite mesobands by backscatter electron scanning electron microscopy (BSE-SEM) reveals internal zonation of magnetite and complex textures in magnetite microlaminae (Figs. 2–5). In mosaic BSE images, the brightness and contrast are distributed by SEM over the full range of grayscale values (8 bits, 256 grays) on all minerals present (Figs. 2a, 3a, 4a, and 5a). Magnetite (Mag) mesobands are composed of multiple ~100 μm thick microlaminae, whereas chert matrix mesobands contain coarse ankerite (Ank) rhombohedra and feathery stilpnomelane (Stp) grains in fine-grained quartz (Qt) matrix. To observe chemical zoning in magnetite, brightness and contrast were adjusted by SEM so the full range of grayscale values was distributed on magnetite only (Figs. 2b, 3b–3c, 4b–4d, and 5b). Quartz, ankerite, and stilpnomelane are present, but appear black in these images.

Energy-dispersive spectroscopy was used to determine the cause of the grayscale variation in BSE-SEM images of magnetite microlaminae. Silicon is the major chemical impurity and is present at higher levels in silician magnetite overgrowths (Si-Mag, dark grays) than in (low-Si) magnetite sub-microlaminae (Mag, light grays). Magnetite domains contain numerous sub-micrometer to micrometer inclusions of carbonate, quartz, stilpnomelane, and apatite (small black dots), whereas silician magnetite overgrowths are euhedral and devoid of mineral inclusions (Figs. 2b, 3b–3c, 4b–4d, and 5b). Silician magnetite overgrowths are zoned in Si, with the highest Si levels at the internal boundary with magnetite and decreasing in Si toward the edge of the overgrowth. In Figure 2b, the uppermost silician magnetite overgrowth shows a step in internal zonation that is also seen for other samples.

We distinguish three distinct textures in magnetite mesobands: (1) magnetite sub-microlaminae with silician magnetite overgrowths, (2) magnetite fragments with silician magnetite overgrowths, and (3) a complex intergrowth of magnetite and silician magnetite (Fig. 4b). In texture 1, magnetite sub-microlaminae may be continuous across millimeter to centimeter wide samples or discontinuous as tens to hundreds of micrometers segments. Magnetite sub-microlaminae are sinuous, typically ~10 to 15 μm thick, and can be resolved into multiple ~5 μm thick layers that are the finest scale of layering described for this BIF (Figs. 3b–3c and 4b–4c). In Figure 3c, these layers are well defined in the upper magnetite sub-microlaminae, whereas in the lower sub-microlaminae, they are less distinct. In Figure 4c, the left side of the image shows two magnetite

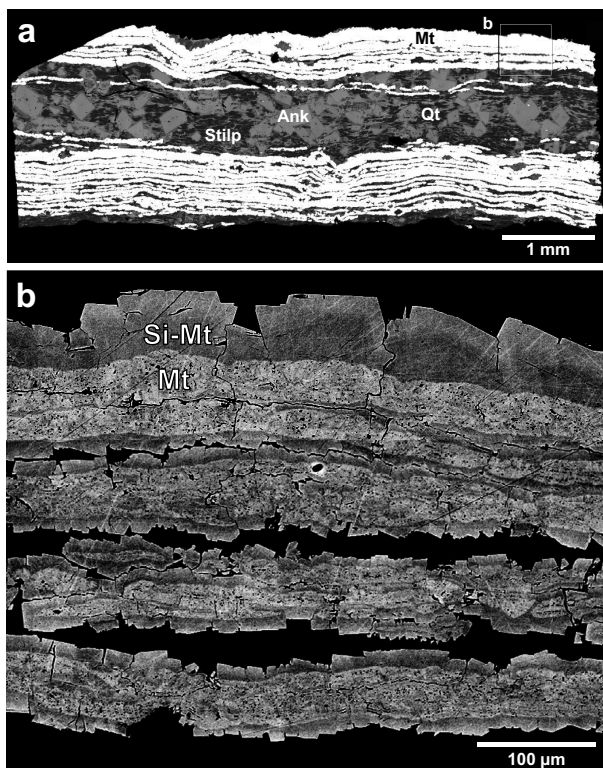


FIGURE 2. BSE images of sample 2-2-a. (a) Mosaic image with brightness and contrast distributed on all minerals present. Magnetite (Mag) mesobands are composed of multiple $\sim 100 \mu\text{m}$ microlaminae while the chert matrix mesoband contains coarse ankerite (Ank) rhombohedra and feathery stilpnomelane (Stp) grains in a fine-grained quartz (Qt) matrix. (b) Brightness and contrast distributed on magnetite only. Magnetite sub-microlaminae are sinuous and contain numerous sub-micrometer to micrometer mineral inclusions (small black dots) while silician magnetite (Si-Mag) overgrowths are euhedral, devoid of mineral inclusions, and zoned in Si from the internal boundary to the edge of the overgrowth.

sub-microlaminae that are each composed of two $\sim 5 \mu\text{m}$ thick layers, whereas on the right side of the image, the two sub-microlaminae join together into a single sub-microlaminae made up of three $\sim 5 \mu\text{m}$ thick layers indicating the loss of one layer. Fine-scale internal layering is only seen in magnetite sub-microlaminae from samples 2-2 and 3-3 in the BIF5 macroband. Texture 1 is found in all BIF samples in this study.

In texture 2, magnetite domains are fragmented, display sharp edges, and are often larger (up to $50 \mu\text{m}$, Figs. 4b, 4d, and 5b) than magnetite sub-microlaminae in texture 1. Magnetite sub-microlaminae and fragments are always surrounded by silician magnetite overgrowths (Figs. 2b, 3b–3c, 4b–4d, and 5b). In texture 3, magnetite and silician magnetite occur as a complex intergrowth at the scale of a few micrometers, and layers are not readily distinguished as in textures 1 and 2 (Fig. 4b). Texture 2 is found in samples 3-3 and 22-3 from the BIF5 and BIF14 macrobands, respectively, and texture 3 is found in sample 3-3 only.

EPMA measurements

To quantify the chemical differences between magnetite and silician magnetite, EPMA measurements were made from multiple traverses and point analyses in samples 2-2, 3-3, 9-12, and 22-3 (Supplemental Table A2¹). Representative traverses are shown in $4 \mu\text{m}$ steps across three magnetite microlaminae for sample 22-3 (Fig. 5b). Silician magnetite overgrowths contain from 1 to 3 wt% SiO_2 , less than 0.5 wt% MgO, and are zoned with the highest amounts of Si and Mg at the inner edge of the overgrowth and decreasing levels to the outer edge (Fig. 5c). SiO_2 and MgO values follow the variation in grayscale values in the BSE image, but MgO is present at 5 to $10\times$ lower levels than SiO_2 .

A total of 316 EPMA measurements were made and are plotted as total cations, $\Sigma(\text{Fe} + \text{Mg}, \text{Zn}, \text{Al}, \text{Ti}, \text{Mn})$, in atoms per formula unit (apfu), on the x-axis against Si apfu on the y-axis (Fig. 6). Ideal magnetite (Fe_3O_4) plots at the origin. Magnesium, Zn, and Mn are assumed to be divalent and substitute into octahedral coordination. Al^{3+} and Ti^{4+} may substitute into either tetrahedral or octahedral coordination. Since Al and Ti are present above detection limits in less than 1/4 of the analyses, the correlation coefficient (R^2) for a linear trend-line changes only in the fifth decimal place when Al and Ti are included with Si on the y-axis. Thus we chose to plot Si alone since it is the major impurity ion and element of interest.

The average values (wt% ± 2 st.dev.) for all data (magnetite and silician magnetite) are: $\text{Fe}_3\text{O}_4 = 98.71 \pm 1.75$, $\text{SiO}_2 = 1.13 \pm 1.19$, $\text{MgO} = 0.12 \pm 0.17$, $\text{ZnO} = 0.18 \pm 0.03$, $\text{Al}_2\text{O}_3 = 0.05 \pm 0.02$, $\text{TiO}_2 = 0.03 \pm 0.02$, and $\text{MnO} = 0.04 \pm 0.01$ (Supplemental Table A2¹). Other than SiO_2 and MgO, the remaining

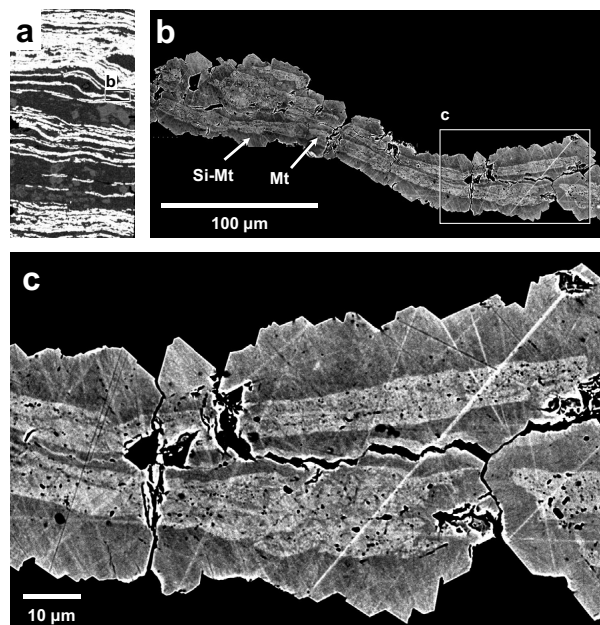


FIGURE 3. BSE images of sample 2-2-b. (a) Mosaic image with brightness and contrast distributed on all minerals present. (b) Brightness and contrast distributed on magnetite only. (c) Individual magnetite sub-microlaminae ~ 10 to $15 \mu\text{m}$ thick are made up of multiple ~ 3 to $5 \mu\text{m}$ thick internal layers.

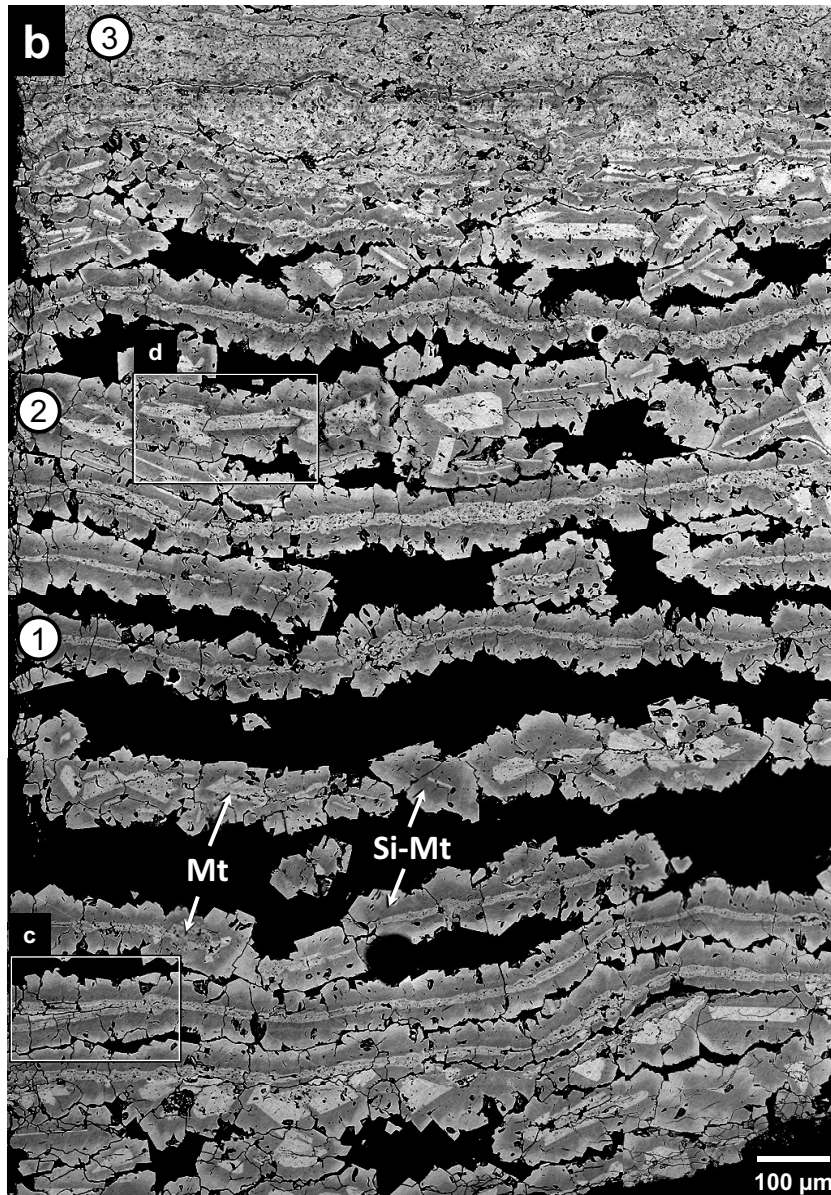
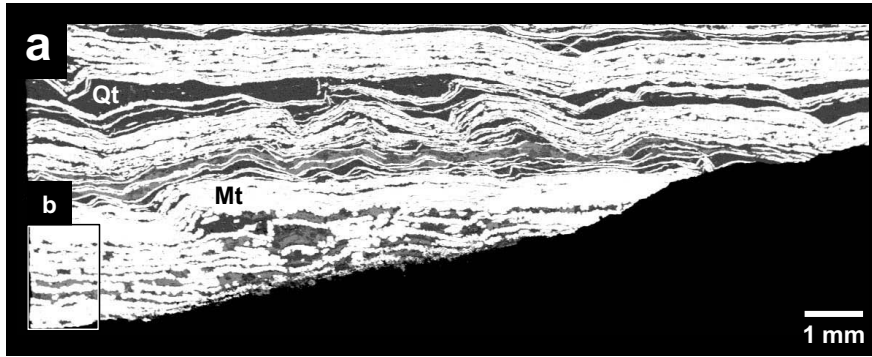


FIGURE 4. BSE images of sample 3-3. **(a)** Mosaic image showing folded magnetite microlaminae. **(b)** Brightness and contrast distributed on magnetite only. Three textures are distinguished in magnetite microlaminae: (1) magnetite sub-microlaminae with silician magnetite overgrowths, (2) recrystallized magnetite fragments with silician magnetite overgrowths, and (3) a complex intergrowth of magnetite and silician magnetite. Magnetite domains are always surrounded by silician magnetite overgrowths. **(c)** Two magnetite sub-microlaminae $\sim 10\text{--}15\ \mu\text{m}$ in size, each made up of two $\sim 5\ \mu\text{m}$ thick layers, join together into a single sub-microlamina made up of three $\sim 5\ \mu\text{m}$ thick layers indicating the loss of one layer. **(d)** Recrystallized magnetite fragments are larger, up to $\sim 50\ \mu\text{m}$ in size, and are variably recrystallized displaying sharp edges.

(continued on next page)

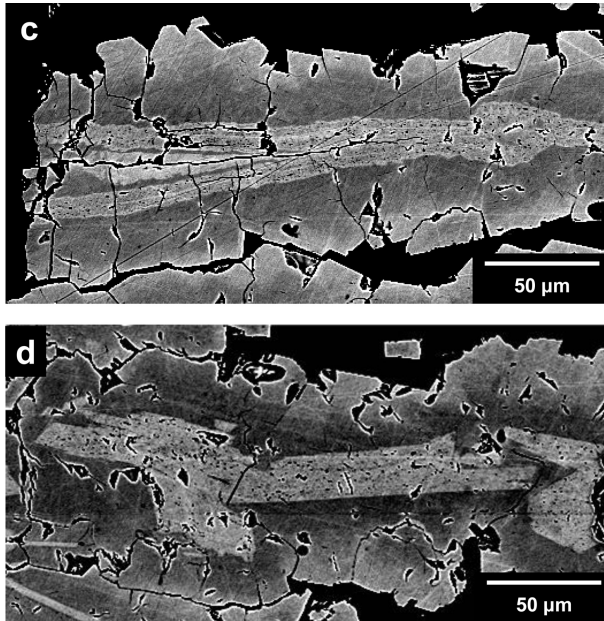


FIGURE 4.—CONTINUED BSE images of sample 3-3. (c) Two magnetite sub-microlaminae $\sim 10\text{--}15\ \mu\text{m}$ in size, each made up of two $\sim 5\ \mu\text{m}$ thick layers, join together into a single sub-microlamina made up of three $\sim 5\ \mu\text{m}$ thick layers indicating the loss of one layer. (d) Recrystallized magnetite fragments are larger, up to $\sim 50\ \mu\text{m}$ in size, and are variably recrystallized displaying sharp edges.

impurities (ZnO, Al_2O_3 , TiO_2 , and MnO) are present at less than 0.2 wt% and average values are close to detection limits from 0.02–0.05 wt% (0.15 wt% for ZnO). There is no difference in MgO content between magnetite and silician magnetite (Supplemental Figure A9). Average values (wt% \pm st.dev.) for magnetite are: $\text{SiO}_2 = 0.58 \pm 0.47$ and $\text{MgO} = 0.11 \pm 0.17$ and for silician magnetite are: $\text{SiO}_2 = 1.43 \pm 1.01$ and $\text{MgO} = 0.11 \pm 0.15$. Silicon was detected in all 316 analyses and Mg was detected in 179 of 316 analyses.

MgO values for magnetite and silician magnetite do vary between different mesoband types. Two rock chips were analyzed from sample 2-2, one from a magnetite mesoband (2-2Z-a) and one from a siderite-rich mesoband (2-2C-b). One rock chip was analyzed from sample 3-3, a magnetite mesoband (3-3A-d). Average MgO values (wt% \pm st.dev.) for all data (magnetite and silician magnetite) are: 0.12 ± 0.17 for sample 2-2Z-a, 0.07 ± 0.04 for sample 2-2C-b, and 0.13 ± 0.19 for sample 3-3A-d (Supplemental Table A2¹). Maximum MgO values (wt%) for all data are: 0.45 for sample 2-2Z-a, 0.11 for sample 2-2C-b, and 0.66 for sample 3-3Z-a. The only other siderite-rich mesoband analyzed in this study is sample 9-12. Average MgO values (wt% \pm st.dev.) for sample 9-12 are 0.08 ± 0.06 and the maximum MgO value (wt%) is 0.15. Thus, MgO values are measurably lower in magnetite from carbonate and siderite-rich mesobands than from magnetite mesobands.

EBSD measurements

Electron backscatter diffraction (EBSD) measurements and orientation contrast (or forescatter) imaging were performed to

determine the crystallographic relationship between magnetite and silician magnetite. A typical orientation contrast image shows differences in grayscale values caused by relative differences in crystallographic orientation and not atomic weight as for BSE (Fig. 7a). Grayscale values show a patchwork texture of single-crystal domains tens of micrometers in size. Inverse pole figures (IPFs) for X, Y, and Z show the crystallographic orientations of single-crystal domains (same colors) relative to the X, Y, and Z direction of the image (Figs. 7b–7d, color scale in Fig. 7e). Pole figures show the sets of planes $\{111\}$, $\{110\}$, and $\{100\}$ in magnetite relative to the sample (Fig. 7f). In Figure 7b, the magnetite microlamina is almost entirely colored red indicating that $\{100\}$ is parallel to the X direction of the image (left to right). Since magnetite is cubic, $\{100\}$ is also normal to the image and sample surface (Fig. 7f). Thus there is a strong preferred orientation for magnetite in the BIF and, by chance, this particular sample was cut parallel to $\{100\}$. Single-crystal domains (same colors) are continuous across the sharp chemical boundary between magnetite and silician magnetite (Figs. 7c–7d). Thus silician magnetite is epitaxial to magnetite.

XRD and TEM analyses

In situ micro-XRD ($\sim 30\ \mu\text{m}$ beam size) was employed to determine if Si solid solution is present in the magnetite crystal structure. In situ XRD analyses were performed on sample 2-2-a, and XRD patterns were refined using Jade 9 software (Materials Data, Inc.). The reference value used for the lattice parameter (a_0) in stoichiometric magnetite is $a_0 = 8.3967(3)\ \text{\AA}$ (Bosi et al. 2009). The most Si-rich XRD analysis has a derived lattice parameter of $a_0 = 8.388(2)\ \text{\AA}$, and the most Si-poor XRD analysis has a derived lattice parameter of $a_0 = 8.392(2)\ \text{\AA}$. In all cases, the derived lattice parameter from the XRD analyses is smaller than the reference value and outside of the uncertainty of the refinement ($\pm 0.002\ \text{\AA}$), which confirms that Si solid solution is present in the magnetite crystal structure. If the presence of Si were due to an admixture of quartz and magnetite at the nanoscale, the lattice parameter for magnetite would not be expected to change. However, the presence of a small, high charge ion like Si in the magnetite crystal structure would decrease the lattice parameter from the reference value as is observed. Octahedral vacancies would similarly result in a decreased lattice parameter.

High-resolution TEM was performed on powder samples from sample 2-2-a. Figure 8 shows a typical TEM bright-field image where the crystal lattice is continuous across the field of view and the diffraction pattern (inset, $[100]$ zone axis) shows reflections $\{hkl\}$ for magnetite only. Silicon is present in spatially resolved chemical analyses as determined by TEM-EDS, and none of the diffraction patterns show any reflections from quartz. Thus TEM verifies that Si solid solution is present in the magnetite crystal structure in agreement with in situ XRD results. Bright and dark patches in the TEM image are not artifacts caused by beam damage but are possibly caused by local chemical differences causing strain contrast and are several unit cells in size. Guinier-Preston (G-P) zone-like textures were seen in a few instances suggesting the presence of nanoscale $\gamma\text{-Fe}_2\text{SiO}_4$ (γ fayalite) domains though Si is dominantly present in solid solution with magnetite.

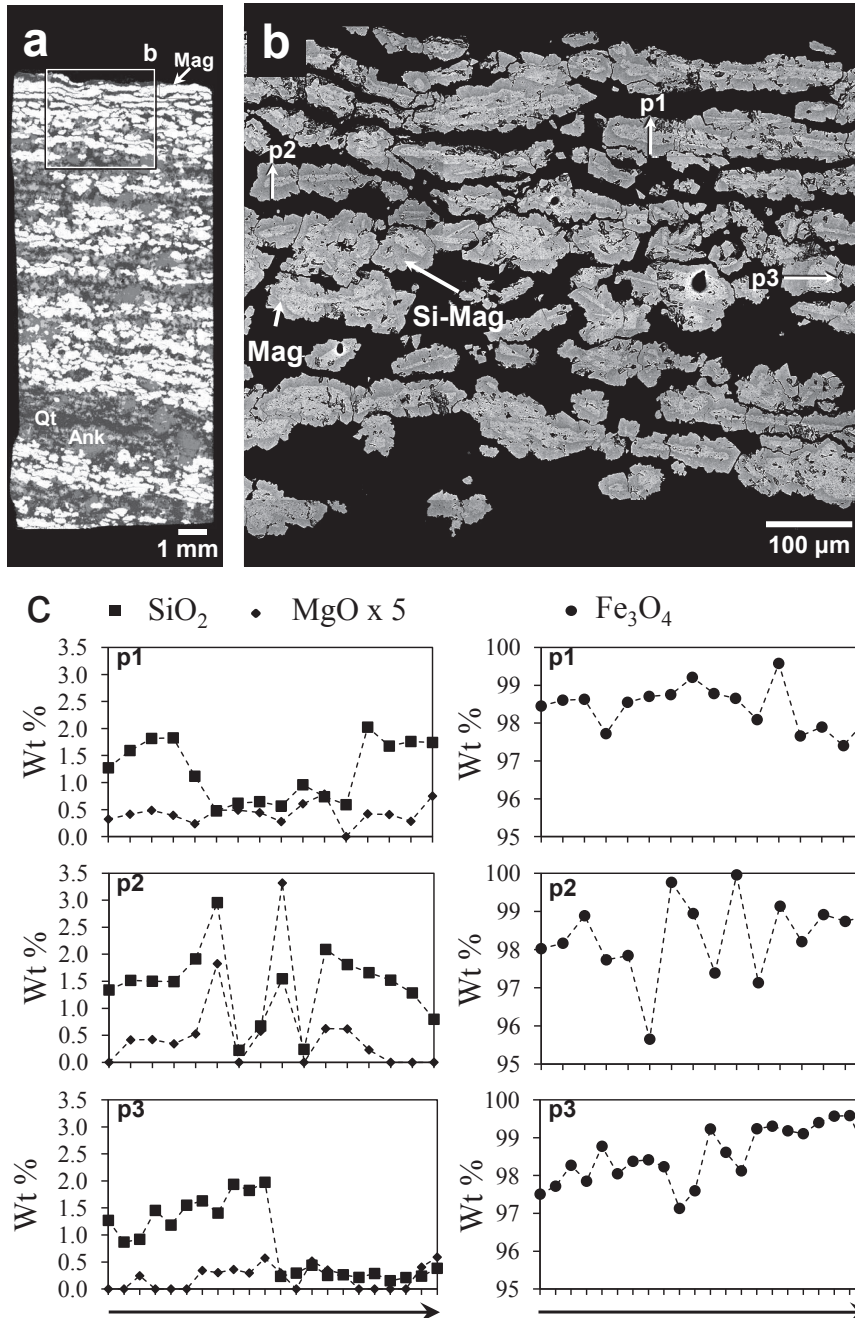


FIGURE 5. BSE images of sample 22-3. (a) Mosaic image of a chert matrix mesoband composed of fragmented magnetite microlaminae with ankerite rhombohedra and fine-grained quartz. (b) Brightness and contrast distributed on magnetite only. (c) EPMA measurements for three traverses (p1 to p3 in b) in 4 μm steps. Silician magnetite contains up to 3 wt% SiO₂, less than 0.5 wt% MgO, and is zoned with the highest amounts of Si and Mg at the boundary between magnetite and silician magnetite. SiO₂ and MgO values follow the variation in grayscale values, but MgO is present at 5 to 10× lower levels than SiO₂.

DISCUSSION

Magnetite relict sedimentary structures and paragenesis

Magnetite domains display relict sedimentary structures formed during soft sediment deformation, whereas silician magnetite overgrowths are either diagenetic or low-temperature

(sub-greenschist facies) burial metamorphic in origin. Relict sedimentary structures include magnetite sub-microlaminae, finer internal layering thereof, and recrystallized magnetite fragments. These are the earliest and best preserved relict sedimentary structures in this BIF and have not been previously described at this level of detail. A paragenetic sequence is established as follows:

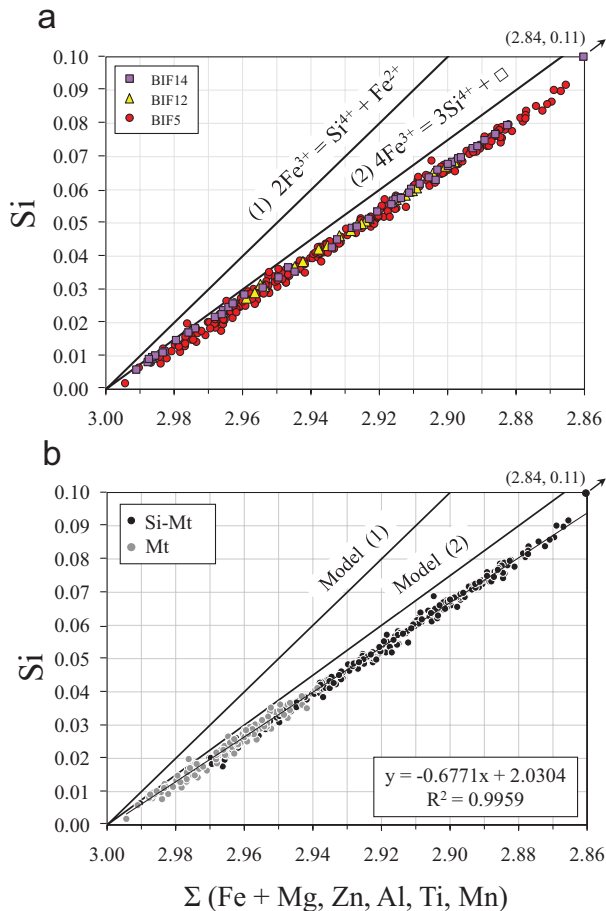


FIGURE 6. EPMA measurements are shown from multiple traverses and point analyses in samples 2-2, 3-3, 9-12, and 22-3 (Fig. 1, Supplemental Table A2¹). (a) EPMA data are plotted as total cations, Σ (Fe + Mg, Zn, Al, Ti, Mn) apfu on the x-axis against Si apfu on the y-axis. Other than SiO_2 and MgO , the remaining impurities (ZnO , Al_2O_3 , TiO_2 , and MnO) are present at less than 0.2 wt% and average values are close to detection limits from 0.02–0.05 wt% (0.15 wt% for ZnO). (b) A linear relation fits the EPMA data exceptionally well ($R^2 = 0.9959$). This relation is close to but reproducibly different from Model 2 especially at higher SiO_2 values. The high precision of the EPMA data suggests a process coupled to the amount of Si to fit Model 2 to the data trend. This difference can be accounted for by a small amount of maghemite substitution coupled to Si content.

(1) Continuous magnetite sub-microlaminae ~ 10 to $15 \mu\text{m}$ thick are preserved with sub-micrometer to micrometer inclusions of quartz, carbonate, stilpnomelane, and apatite. Sub-microlaminae are composed of internal layers $\sim 5 \mu\text{m}$ thick.

(2) Magnetite sub-microlaminae are selectively preserved as discontinuous tens to hundreds of micrometers segments.

(3) Magnetite sub-microlaminae variably recrystallize into larger $\sim 50 \mu\text{m}$ fragments.

(4) Silician magnetite overgrowths form surrounding all magnetite domains including sub-microlaminae and fragments.

We interpret magnetite textures formed by steps 1–3 as relict sedimentary layering of primary origin. However, we do not consider magnetite as the primary mineral since most BIF minerals

are the products of dehydration, diagenesis, and metamorphism. Magnetite textures formed by steps 1–2 are classified as texture 1. In step 3, local recrystallization of magnetite domains is classified as texture 2. This is the most striking example of soft sediment deformation of magnetite. We suggest that these fragments were formerly parts of magnetite sub-microlaminae since they still contain sub-micrometer to micrometer mineral inclusions. Textures 1 and 2 alternate between successive microlaminae, thus recrystallization was confined to individual microlaminae on a $\sim 100 \mu\text{m}$ scale (Fig. 4b).

Recrystallized magnetite fragments contain fewer mineral inclusions than magnetite sub-microlaminae. We hypothesize that magnetite sub-microlaminae may have initially formed containing variable amounts of mineral inclusions. Magnetite sub-microlaminae with fewer inclusions may have recrystallized more easily (texture 2) than sub-microlaminae where the grain-boundary pinning effects of a greater number of inclusions (texture 1) restricted recrystallization of magnetite. Alternatively, some of the inclusions may have been removed during recrystallization.

Silician magnetite overgrowths formed in step 4 do not show relict sedimentary textures as are seen for magnetite. Silician magnetite is zoned in Si and does not contain mineral inclusions unlike magnetite domains. We suggest that silician magnetite formed from Si-bearing fluids that dissolved prior magnetite and reprecipitated it under conditions that stabilized silician magnetite.

Crystal chemistry of silician magnetite

EBSD analyses show that single-crystal domains are continuous across the sharp chemical boundary between magnetite domains and silician magnetite overgrowths (Figs. 7b–7d). Silician magnetite is epitaxial to magnetite, which suggests that magnetite had already formed to serve as a nucleating surface for the silician magnetite overgrowths. Silicon solid solution is present in the magnetite crystal structure as determined by in situ micro-XRD and TEM analyses. Our XRD results [max. 3.0 wt% SiO_2 , $a_o = 8.388(2) \text{ \AA}$] agree with those reported for silician magnetite [max. 3.8 wt% SiO_2 , $a_o = 8.376(1) \text{ \AA}$] from the Kumano skarn, Japan (Ohkawa et al. 2007). Newberry et al. (1982) used TEM and reported silician magnetite intergrowths with ilmenite in titanomagnetite phenocrysts from Mickey Pass Tuff, Nevada.

We observed silician magnetite in all 11 samples (2-2 to 32-3) from 6 BIF macrobands (BIF5, 12-16) in the Dales Gorge type-section drill core DDH-47A at Wittenoom. Assuming these samples are representative, silician magnetite is the dominant iron oxide and is ubiquitous in the Dales Gorge BIF. Morris (1991) observed that zonation in magnetite microlaminae from drill core DDH-44 at Paraburadoo was due to differences in Si content, whereas Pecoits et al. (2009) reported up to 2 wt% SiO_2 in magnetite from DDH-44 using EPMA. Additionally, we have found silician magnetite overgrowths on magnetite by BSE-SEM in BIFs from the ~ 2.5 Ga Weeli Wolli Formation, Hamersley Group, Western Australia, the ~ 1.9 Ga Biwabik Iron Formation, Minnesota, U.S.A., and the ~ 1.6 Ga Freedom Iron Formation, Wisconsin, U.S.A. Thus, silician magnetite may be a common feature of low-temperature metamorphosed BIFs worldwide.

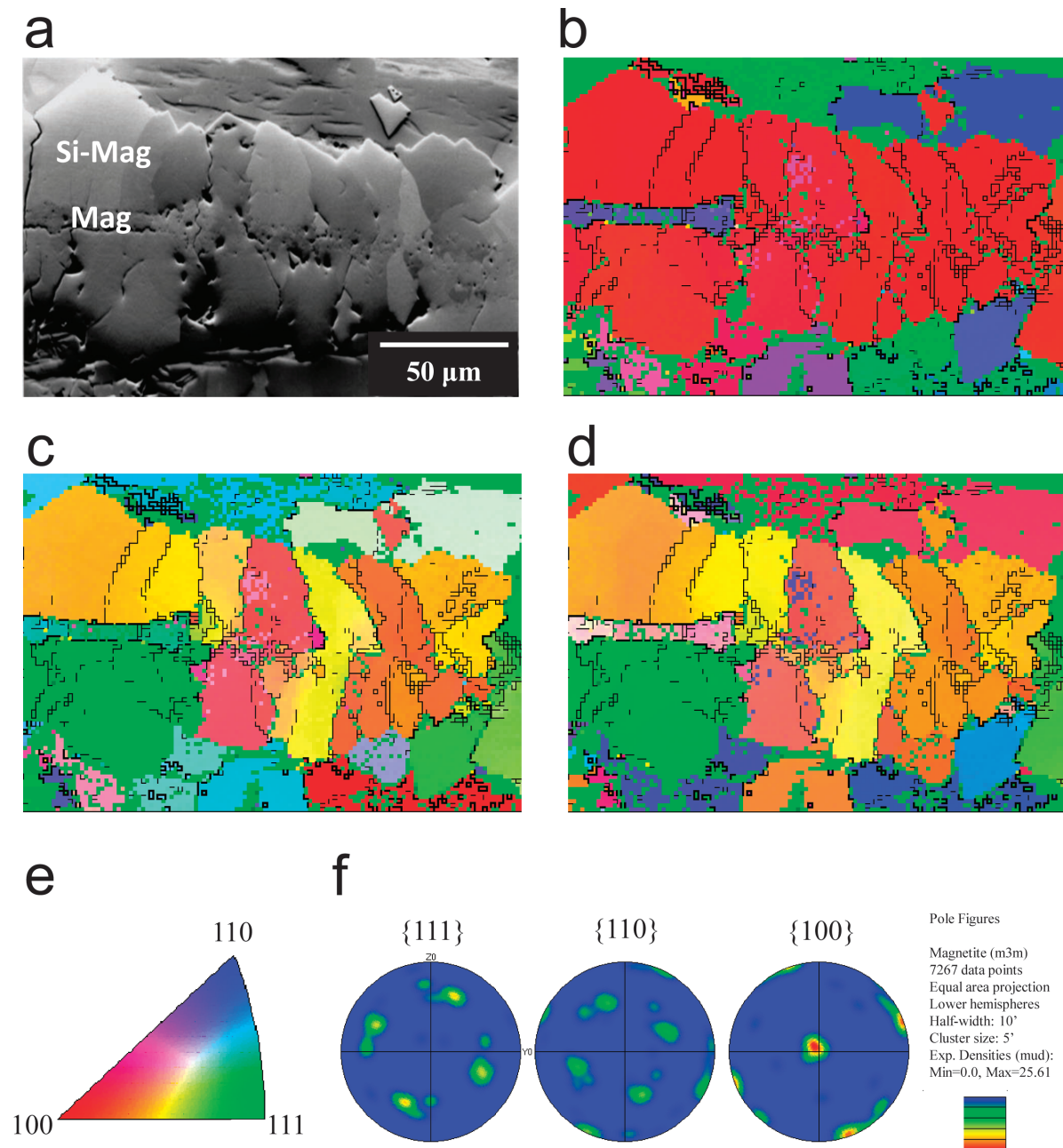


FIGURE 7. (a) Orientation contrast (OC, or forescatter) image from sample 3-3. Grayscale values show a patchwork texture of single-crystal domains up to tens of micrometers in size. (b–e) Inverse pole figures (IPFs) for X, Y, and Z (b, c, and d respectively; color scale, e) show the crystallographic orientations of single-crystal domains (same colors) relative to the X, Y, and Z direction of the image. (b) Magnetite microlaminae are colored almost entirely red indicating that {100} is parallel to the X direction of the image (left to right). (c–d) Single-crystal domains (same colors) are continuous across the sharp chemical boundary between magnetite and silician magnetite. (f) Pole figures show the three primary sets of planes, {111}, {110}, and {100}, in magnetite relative to the sample. There is a strong preferred orientation for magnetite in the BIF and by chance, this particular sample was cut nearly parallel to {100}.

Solid-solution models

Magnetite has an inverse-spinel crystal structure consisting of alternating tetrahedral (IV) and octahedral (VI) layers along the $\langle 111 \rangle$ set of directions. Each unit cell contains eight formula units consisting of three cations per four oxygen atoms with an ideal formula as follows



We suggest three coupled substitutions (models) for Si solid solution in magnetite. The $^{\text{IV}}\text{Si}^{4+}$ ion has a small ionic radius (0.26 Å) (Shannon 1976) compared to $^{\text{IV}}\text{Fe}^{3+}$ (0.57 Å), $^{\text{VI}}\text{Fe}^{3+}$

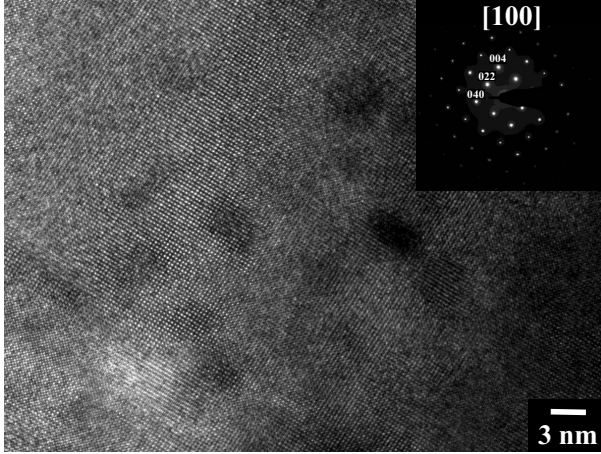


FIGURE 8. Typical high-resolution bright-field TEM image where the crystal lattice is continuous across the field of view and the diffraction pattern (inset, [100] zone axis) shows reflections $\{hkl\}$ for magnetite only. Silicon is present in spatially resolved analyses as determined by TEM-EDS. TEM verifies Si solid solution is present in the magnetite crystal structure. Bright and dark patches in the TEM image are not artifacts caused by beam damage but are likely due to local chemical differences causing strain contrast and are several unit cells in size.

(0.63 Å), and $^{VI}Fe^{2+}$ (0.71 Å) (Whittaker and Muntus 1970) and thus substitutes into tetrahedral coordination.

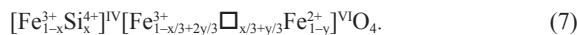
In Model 1, each Si^{4+} ion couples with one Fe^{2+} to replace two Fe^{3+} ions



In Model 2, three Si^{4+} ions couple with one octahedral vacancy (\square) to replace four Fe^{3+} ions.



Similar to the octahedral substitution in Equation 4, additional vacancies may be present in maghemite substitution. In Model 3, three Si^{4+} ions couple with one octahedral vacancy to replace four Fe^{3+} ions and two Fe^{3+} ions couple with one octahedral vacancy for three Fe^{2+} ions.



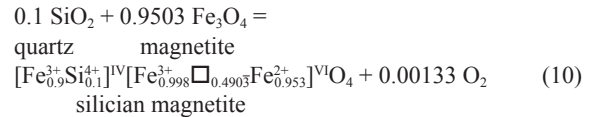
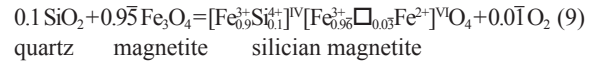
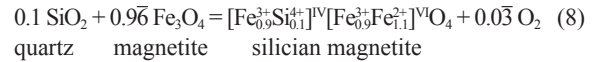
Comparison of EPMA data to solid-solution models

The EPMA data fit a linear relation exceptionally well ($R^2 = 0.9959$, Fig. 6b). This relation is close to but reproducibly different from Model 2 especially at higher SiO_2 values (Fig. 6). There are several reasons why Model 2 might not fit the data exactly including uncertainties in the analysis, undetected

elements, and additional vacancy substitutions. Two magnetite standards were used during EPMA: a natural magnetite and a synthetic magnetite. The $FeK\alpha$ counts for the natural magnetite are slightly lower than for the synthetic magnetite. All our data are calculated relative to the natural magnetite, and if calculated relative to synthetic magnetite, the Fe atoms would increase by 0.001, which is not enough to make up for the difference between Model 2 and the linear fit to the data. Another uncertainty is that oxygen was not analyzed directly, thus if magnetite was oxygen deficient ($Fe:O > 0.75$), this would increase the number of calculated formula atoms.

Other than the elements reported here (Fe, Si, Mg, Zn, Al, Ti, and Mn), V and Cr were analyzed for but not detected, and even if other elements were present near detection limits, there would need to be about 10 unanalyzed elements. A further uncertainty lies in the assumption of a stoichiometric $Fe^{3+}:Fe^{2+}$ ratio of 2:1 for distributing the charge to Fe in magnetite for the EPMA data. However given the complex textures, it would be difficult to measure the $Fe^{3+}:Fe^{2+}$ ratio in situ for these samples.

The high precision of the EPMA data suggests a process coupled to the amount of Si to fit Model 2 to the data trend. This difference can be accounted for by a small amount of maghemite substitution in Model 3. The amount of maghemite would be a function of Si content, and the ratio of octahedral vacancies x to y needed is ~ 10 to 1 (Eqs. 6–7). For silician magnetite with 0.1 Si apfu, the equations for quartz plus magnetite equal silician magnetite using the substitutions in Models 1, 2, and 3, respectively, are as follows. Overbars indicate repeating decimals.



All three solid substitutions show that silician magnetite is stabilized relative to magnetite (+quartz) by more reducing conditions than for (low-Si) magnetite.

Silician magnetite as a potential biosignature in BIFs

Magnetite has long been considered evidence for the former presence of organic carbon in BIFs (e.g., French 1968; Klein 1973). Typically, only low amounts of organic carbon (< 1 wt% C) are found in oxide-facies BIFs, whereas up to several weight percent of organic carbon are reported in carbonate-facies BIFs (Klein 2005). French (1968) mapped the metamorphic isograd hematite + C = magnetite + CO_2 in the Biwabik Iron Formation. Thus, organic carbon was required to reduce hematite to magnetite. Assuming the BIF oxide precipitate was ferric oxide/hydroxide and was converted to magnetite, there must have been a source of reduction. Organic carbon is the most reasonable cause of this reaction, thus any magnetite is a potential biosignature in BIFs.

We hypothesize that silician magnetite is also a potential biosignature in BIFs and suggest that excess organic carbon remained after formation of magnetite sub-microlaminae. The former presence of this organic carbon stabilized silician magnetite under reducing conditions that occurred during diagenesis and burial metamorphism. Thus, the stability of silician magnetite extends to slightly lower oxygen fugacities than for pure magnetite (+quartz).

Selective oxidation of magnetite to hematite

Magnetite microlaminae containing hematite sub-microlaminae has been reported by previous studies of the Dales Gorge BIF from drill core DDH-44 at Paraburdoo (Morris 1980, 1991, 1993; Ewers and Morris 1981; Pecoits et al. 2009; Steinhofel et al. 2010). Ewers and Morris (1981) reported hematite sub-microlaminae in magnetite microlaminae similar to texture 1 from this study. Importantly, no hematite sub-microlaminae are seen in equivalent magnetite microlaminae from drill core DDH-47A at Wittenoom and at other localities. Ewers and Morris (1981) interpret hematite sub-microlaminae at Paraburdoo to have formed prior to (silician) magnetite overgrowths and the lack of hematite sub-microlaminae (thus greater magnetite) at Wittenoom to indicate increasing metamorphic grade in the order: Paraburdoo, Wittenoom. By contrast, Smith et al. (1982) defined metamorphic zones by the silicate mineralogy of volcanic rocks in the Fortescue Group that indicate increasing grade in the order: Wittenoom, Paraburdoo, Tom Price.

Why are there hematite sub-microlaminae at Paraburdoo but not at Wittenoom or any other localities of the Dales Gorge BIF? We consider three possibilities: (1) hematite formed prior to magnetite, (2) a lack of organic matter resulted in the formation of hematite, or (3) magnetite was selectively oxidized to hematite. First, if hematite formed prior to magnetite, this would require oxidizing conditions in the sediment column during precipitation and/or diagenesis. At Paraburdoo, hematite sub-microlaminae are always surrounded by silician magnetite overgrowths (Morris 1991) that we interpret to be diagenetic in origin and indicative of reduction, likely resulting from the former presence of organic carbon. If magnetite sub-microlaminae at Wittenoom formed by partial reaction of prior hematite, we would not expect to see sharp linear boundaries between the two minerals as are observed for all samples in this study. Second, hematite sub-microlaminae at Paraburdoo may have formed due to a lack of organic matter, thus exhausting the hematite + C = magnetite + CO₂ buffer and resulting in residual hematite.

A third possibility is that hematite sub-microlaminae may have formed by selective oxidation of prior magnetite during diagenesis and burial metamorphism. Han (1978, 1982) described natural and induced partial oxidation textures of magnetite containing hematite from diverse BIFs worldwide. Rapid laboratory experiments in air (Han 1978, 1982) were used to oxidize magnetite to hematite (300 °C for several days) and yielded results similar to naturally occurring examples of magnetite containing hematite some of which are comparable to texture 1 from this study. Han (1978) interpreted natural and induced hematite domains as having formed prior to magnetite although he did not explain why magnetite was only selectively oxidized rather than completely transformed to hematite.

We suggest that Si solid solution in the magnetite lattice inhibits the transformation of magnetite to hematite during diagenesis and burial metamorphism of BIFs. Laboratory studies on the catalytic interactions between silica and magnetite support this hypothesis. Synthetic lab experiments by Lund and Dumesic (1981) found that the phase transformation of magnetite to hematite in air was inhibited for silician magnetite and instead resulted in the formation of maghemite at temperatures up to 550 °C. We hypothesize that examples of natural and synthetic selective oxidation of magnetite to hematite in BIFs may be evidence that only magnetite with low Si content transformed to hematite and the remaining magnetite was stabilized by its higher Si content and thus did not transform to hematite. The presence of hematite sub-microlaminae with silician magnetite overgrowths at Paraburdoo can be explained by selective oxidation of low-Si magnetite by burial metamorphic fluids at this particular location, whereas at all other localities (including Wittenoom), magnetite laminae surrounded by silician magnetite overgrowths were preserved indicating that magnetite formed prior to hematite.

ACKNOWLEDGMENTS

We thank Alec Trendall and Richard Morris for conversations during the 5th International Archean Symposium. Richard Morris helped authenticate our samples. We thank Cornelius (Kase) Klein, Clark Johnson, and the UW-Madison Geology Museum for providing the drill core samples used in this study. We thank Brian Hess for sample preparation and Phil Brown and Chloë Bonamici for helpful conversations. Reviews by Phillip Fralick and Nicolaus Dauphas substantially improved this paper. This study was funded by the NASA Astrobiology Institute (N07-5489), NSF-EAR (0509639, 0838058, 0619368), and DOE (93ER 14389, 09ER 16050).

REFERENCES CITED

- Armstrong, J.T. (1988) Quantitative analysis of silicates and oxide minerals: comparison of Monte Carlo, ZAF and phi-rho-z procedures. In D.E. Newbury, Ed., *Microbeam Analysis*, p. 239–246. San Francisco Press, California.
- Ayres, D.E. (1972) Genesis of iron-bearing minerals in banded iron formation mesobands in the Dales Gorge member, Hamersley Group, Western Australia. *Economic Geology*, 67, 1214–1233.
- Bekker, A., Slack, J.F., Planavsky, N., Krapež, B., Hofmann, A., Konhauser, K.O., and Rouxel, O.J. (2010) Iron formation: The sedimentary product of a complex interplay among mantle, tectonic, oceanic, and biospheric processes. *Economic Geology*, 105, 467–508.
- Blockley, J.G., Morris, R.C., and Trendall, A.F. (2008) History and significance of drillcore from the Brockman Iron Formation forming the lift panels on the fifth floor of Mineral House, Perth. *Geological Survey of Western Australia, Record 2007/18*, 15p.
- Bosi, F., Hälenius, U., and Skogby, H. (2009) Crystal chemistry of the magnetite-ulvöspinel series. *American Mineralogist*, 94, 181–189.
- Craddock, P.R. and Dauphas, N. (2011) Iron and carbon isotope evidence for microbial iron respiration throughout the Archean. *Earth and Planetary Science Letters*, 303, 121–132.
- Czaja, A.D., Johnson, C.M., Beard, B.L., Eigenbrode, J.L., Freeman, K.H., and Yamaguchi, K.E. (2010) Iron and carbon isotope evidence for ecosystem and environmental diversity in the <2.7 to 2.5 Ga Hamersley Province, Western Australia. *Earth and Planetary Science Letters*, 292, 170–180.
- Donovan, J.J., Kremser, D., and Fournelle, J.H. (2010) Probe for EPMA v. 8.24 User's Guide and Reference, Enterprise Edition, 398 pp.
- Ewers, W.E. and Morris, R.C. (1981) Studies of the Dales Gorge Member of the Brockman Iron Formation, Western Australia. *Economic Geology*, 76, 1929–1953.
- Fischer, W.W. and Knoll, A.H. (2009) An iron shuttle for deepwater silica in Late Archean and early Paleoproterozoic iron formation. *Geological Society of America Bulletin*, 121, 222–235.
- French, B.M. (1968) Progressive contact metamorphism of the Biwabik iron formation, Mesabi Range, Minnesota. *Minnesota Geological Survey Bulletin*, 45, 1–103.
- Han, T.-M. (1978) Microstructures of magnetite as guides to its origin in some Precambrian iron-formations. *Fortschritte der Mineralogie*, 56, 105–142.
- (1982) Iron formations of Precambrian age: Hematite-magnetite relationships in some Proterozoic iron deposits—A microscopic observation. In G.C. Amstutz, A. El Goresy, G. Frenzel, C. Kluth, G. Moh, A. Wauschkuhn, and

- R.A. Zimmerman, Eds., *Ore Genesis: The State of the Art*, p. 451–459. Special Publication No. 2 of the Society for Geology Applied to Mineral Deposits, Springer-Verlag, New York.
- Harder, H. (1965) Experimente zur "Ausfällung" der Kieselsäure. *Geochimica et Cosmochimica Acta*, 29, 429–442 (in German).
- Harder, H. and Flehmig, W. (1970) Quarzsynthese bei tiefen Temperaturen. *Geochimica et Cosmochimica Acta*, 34, 295–305 (in German).
- Heck, P.R., Huberty, J.M., Kita, N.T., Ushikubo, T., Kozdon, R., and Valley, J.W. (2011) SIMS analyses of silicon and oxygen isotope ratios for quartz from Archean and Paleoproterozoic banded iron formations. *Geochimica et Cosmochimica Acta*, 75, 5879–5891.
- Heimann, A., Johnson, C.M., Beard, B.L., Valley, J.W., Roden, E.E., Spicuzza, M.J., and Beukes, N.J. (2010) Fe, C, and O isotope compositions of banded iron formation carbonates demonstrate a major role for dissimilatory iron reduction in ~2.5 Ga marine environments. *Earth and Planetary Science Letters*, 294, 8–18.
- James, H.L. (1954) Sedimentary facies of iron-formation. *Economic Geology*, 49, 235–293.
- Johnson, C.M., Beard, B.L., Klein, C., Beukes, N.J., and Roden, E.E. (2008) Iron isotopes constrain biologic and abiologic processes in banded iron formation genesis. *Geochimica et Cosmochimica Acta*, 72, 151–169.
- Klein, C. (1973) Changes in mineral assemblages with metamorphism of some banded Precambrian iron-formations. *Economic Geology*, 68, 1075–1088.
- (2005) Some Precambrian banded iron-formations (BIFs) from around the world: Their age, geologic setting, mineralogy, metamorphism, geochemistry, and origin. *American Mineralogist*, 90, 1473–1499.
- Koehler, I., Konhauser, K., and Kappler, A. (2010) Role of microorganisms in banded iron formations. In A. Loy, M. Mandl, and L.L. Barton, Eds., *Geomicrobiology: Molecular and Environmental Perspective*, p. 309–324. Springer, Dordrecht.
- Konhauser, K.O., Newman, D.K., and Kappler, A. (2005) The potential significance of microbial Fe(III) reduction during deposition of Precambrian banded iron formations. *Geobiology*, 3, 167–177.
- Krapež, B., Barley, M.E., and Pickard, A.L. (2003) Hydrothermal and resedimented origins of the precursor sediments to banded iron formation: sedimentological evidence from the Early Palaeoproterozoic Brockman Supersequence of Western Australia. *Sedimentology*, 50, 979–1011.
- Kukkapudu, R.V., Zachara, J.M., Fredrickson, J.K., and Kennedy, D.W. (2004) Biotransformation of two-line silica-ferrihydrite by a dissimilatory Fe(III)-reducing bacterium: Formation of carbonate green rust in the presence of phosphate. *Geochimica et Cosmochimica Acta*, 68, 2799–2814.
- Lund, C.R.F. and Dumesic, J.A. (1981) Strong oxide-oxide interactions in silica-supported magnetite catalysts. 1. X-ray diffraction and Mössbauer spectroscopy evidence for interaction. *Journal of Physical Chemistry*, 85, 3175–3180.
- Morris, R.C. (1973) A pilot study of phosphorous distribution in parts of the Brockman Iron Formation, Hamersley Group, Western Australia. *Geological Survey, Annual Report*, 1972, 75–80.
- (1980) A Textural and mineralogical study of the relationship of iron ore to banded iron-formation in the Hamersley Iron Province of Western Australia. *Economic Geology*, 75, 184–209.
- (1991) The Marra Mamba Iron Formation of the Hamersley Group of Western Australia. CSIRO/AMIRA Iron Ores of the Hamersley Province Project P75F, Exploration Geoscience Restricted Report 158R, 229 p.
- (1993) Genetic modelling for banded iron-formation of the Hamersley Group, Pilbara Craton, Western Australia. *Precambrian Research*, 60, 243–286.
- Newberry, N.G., Peacor, D.R., Essene, E.J., and Geissman, J.W. (1982) Silicon in magnetite: High-Resolution microanalysis of magnetite-ilmenite intergrowths. *Contributions to Mineralogy and Petrology*, 80, 334–340.
- Ohkawa, M., Miyahara, M., Ohta, E., and Hoshino, K. (2007) Silicon-substituted magnetite and accompanying iron oxides and hydroxides from the Kumano mine, Yamaguchi Prefecture, Japan: Reexamination of the so-called maghemite (γ -Fe₂O₃). *Journal of Mineralogical and Petrological Sciences*, 102, 182–193.
- Ohmoto, H., Watanabe, Y., Yamaguchi, K., Naraoka, H., Haruna, M., Kakegawa, T., Hayashi, K.-I. and Kato, T. (2006) Chemical and biological evolution of early Earth: Constraints from banded iron formations. In S.E. Kesler, and H. Ohmoto, Eds., *Evolution of Early Earth's Atmosphere, Hydrosphere, and Biosphere—Constraints from Ore Deposits*, 198, p. 291–331. Geological Society of America Memoir, Boulder, Colorado.
- Pecoits, E., Gringas, M.K., Barley, M.E., Kappler, A., Posth, N.R., and Konhauser, K.O. (2009) Petrography and geochemistry of the Dales Gorge banded iron formation: Paragenetic sequence, source and implications for palaeo-ocean chemistry. *Precambrian Research*, 172, 163–187.
- Pickard, A.L., Barley, M.E., and Krapež, B. (2004) Deep-marine depositional setting of banded iron formation: sedimentological evidence from interbedded clastic sedimentary rocks in the early Palaeoproterozoic Dales Gorge Member of Western Australia. *Sedimentary Geology*, 170, 37–62.
- Posth, N.R., Hegler, F., Konhauser, K.O., and Kappler, A. (2008) Alternating Si and Fe deposition caused by temperature fluctuations in Precambrian oceans. *Nature Geoscience*, 1, 703–708.
- Shannon, R.D. (1976) Revised effective ionic radii and systematic studies of interatomic distances in halides and chalcogenides. *Acta Crystallographica*, A32, 751–767.
- Shimazaki, H. (1998) On the occurrence of silician magnetites. *Resource Geology*, 48, 23–29.
- Smith, R.E., Perdix, J.L., and Parks, T.C. (1982) Burial metamorphism in the Hamersley Basin, Western Australia. *Journal of Petrology*, 23, 75–102.
- Steinboedel, G., Horn, I., and Blanckenburg, F. (2009) Micro-scale tracing of Fe and Si isotope signatures in banded iron formation using femtosecond laser ablation. *Geochimica et Cosmochimica Acta*, 73, 5343–5360.
- Steinboedel, G., von Blanckenburg, F., Horn, I., Konhauser, K.O., Beukes, N.J. and Gutzman, J. (2010) Deciphering formation processes of banded iron formations from the Transvaal and the Hamersley successions by combined Si and Fe isotope analysis using UV femtosecond laser ablation. *Geochimica et Cosmochimica Acta*, 74, 2677–2696.
- Trendall, A.F. (1973) Varve cycles in the Weeli Wolli Formation of the Precambrian Hamersley Group, Western Australia. *Economic Geology*, 68, 1089–1097.
- (2002) The significance of iron-formation in the Precambrian stratigraphic record. In W. Altermann and P.L. Corcoran, Eds., *Precambrian Sedimentary Environments: A Modern Approach to Depositional Systems*, p. 33–66. International Association of Sedimentologists Special Publication 33. Wiley, New York.
- Trendall, A.F. and Blockley, J.G. (1968) Stratigraphy of the Dales Gorge Member of the Brockman Iron Formation in the Precambrian Hamersley Group of Western Australia. *Geological Survey of Western Australia Annual Report for 1967*, p. 48–53.
- (1970) The iron formations of the Precambrian Hamersley Group, Western Australia with special reference to the associated crocidolite. *Geological Survey of Western Australia Bulletin* 119, East Perth.
- Trendall, A.F., Compston, W., Nelson, D.R., De Laeter, J.R., and Bennet, V.C. (2004) SHRIMP zircon ages constraining the depositional chronology of the Hamersley Group, Western Australia. *Australian Journal of Earth Sciences*, 51, 621–644.
- Wang, Y., Xu, H., Merino, E., and Konishi, H. (2009) Generation of banded iron formations by internal dynamics and leaching of oceanic crust. *Nature Geoscience*, 2, 781–784.
- Whittaker, E.J.W. and Muntus, R. (1970) Ionic radii for use in geochemistry. *Geochimica et Cosmochimica Acta*, 34, 945–956.
- Wu, L., Beard, B.L., Roden, E.E., and Johnson, C.M. (2009) Influence of pH and dissolved Si on Fe isotope fractionation during dissimilatory microbial reduction of hematite. *Geochimica et Cosmochimica Acta*, 73, 5584–5599.
- Yokoyama, T., Nakazato, T., and Tarutani, T. (1980) Polymerization of silicic acid adsorbed on iron (III) hydroxide. *Bulletin of the Chemical Society of Japan*, 53, 850–853.
- Yokoyama, T., Shimono, T., and Tarutani, T. (1984) Study of the polymerization of silicic acid adsorbed on iron (III) hydroxide by trimethylsilylation-gas chromatography. *Bulletin of the Chemical Society of Japan*, 57, 2315–2316.

MANUSCRIPT RECEIVED APRIL 19, 2011

MANUSCRIPT ACCEPTED SEPTEMBER 26, 2011

MANUSCRIPT HANDLED BY M. DARBY DYAR